

Thermophysical modeling of selective laser ablation processing of lithium-ion battery cathodes

Cite as: J. Laser Appl. **32**, 042008 (2020); <https://doi.org/10.2351/7.0000200>

Submitted: 10 July 2020 . Accepted: 12 September 2020 . Published Online: 28 September 2020

Sebastian Enderle, Marius Bolsinger, Simon Ruck, Volker Knoblauch , and Harald Riegel 



View Online



Export Citation



CrossMark

ARTICLES YOU MAY BE INTERESTED IN

[Crystal alignment of a \$\text{LiNi}_{0.5}\text{Mn}_{0.3}\text{Co}_{0.2}\text{O}_2\$ electrode material for lithium ion batteries using its magnetic properties](#)

Applied Physics Letters **117**, 123903 (2020); <https://doi.org/10.1063/5.0016456>

[Impact of laser beam oscillation strategies on surface treatment of microalloyed steel](#)

Journal of Laser Applications **32**, 042006 (2020); <https://doi.org/10.2351/7.0000196>

ALIA



OCTOBER 19-20, 2020
A VIRTUAL CONFERENCE ON
LASERS AND ELECTRO-OPTICS

Thermophysical modeling of selective laser ablation processing of lithium-ion battery cathodes

Cite as: J. Laser Appl. 32, 042008 (2020); doi: 10.2351/7.0000200

Submitted: 10 July 2020 · Accepted: 12 September 2020 ·

Published Online: 28 September 2020



Sebastian Enderle,^{1,a)} Marius Bolsinger,² Simon Ruck,¹ Volker Knoblauch,²  and Harald Riegel¹ 

AFFILIATIONS

¹Laser Application Center, Aalen University, Beethovenstr. 1, D-73430 Aalen, Germany

²Materials Research Institute Aalen, Aalen University, Beethovenstr. 1, D-73430 Aalen, Germany

^{a)}Author to whom correspondence should be addressed; electronic mail: Sebastian.enderle@hs-aalen.de

ABSTRACT

The microstructural optimization of lithium-ion battery (LiB) electrodes has recently gained a lot of interest. Versatile approaches to enhance fast charging abilities of LiB electrodes are the subject of current research. One of these approaches is the laser based photothermic removal of superficial inactive electrode components in order to improve the accessibility of the active material particles for the lithium-ions. In this work, we established a thermophysical model to describe the temperature fields within the electrode resulting from laser material processing. The model delivers satisfying results regarding the prediction of the removal of the top surface electrode layer that mainly consists of a binder and conductive additives. Lining up a simple approach of estimating the average depth in which the inactive binder-additive compound is selectively removed from the electrode's active mass layer led to a good agreement between the calculated and experimental results. Additionally, a potential negative thermal impact on the active material particles themselves due to the laser processing is evaluated. The established model can be used to optimize laser parameters in order to simultaneously maximize the selectively ablated inactive material and to minimize the thermal impact on the active material particles. Moreover, the model is capable of being transferred to laser processing of other types of composite materials such as LiB-anodes or carbon fiber reinforced polymers.

Key words: lithium-ion battery, cathode, rate capability, binder ablation, selective laser ablation, thermophysical modeling

Published under license by Laser Institute of America. <https://doi.org/10.2351/7.0000200>

I. INTRODUCTION

In the automotive sector, the lithium-ion battery (LiB) technology has recently gained major attention. Despite the high energy and power densities that lithium-ion batteries are offering, they are still facing an immense drawback compared with conventional combustion fuels as energy storage, namely, the charging time. Besides the influences of the battery system design, the fast charging ability is highly influenced by the cell chemistry and microstructural properties of the electrodes within each battery cell.^{1–3} Current research activities are investigating laser based surface modification and structuring methods in order to optimize the electrodes microstructure and thus allowing high current rates at reasonable charging capacity.^{4–8}

Fast charging means that high current rates are applied and a high number of Li-ions need to be (de)intercalated in the active materials and transferred between the electrodes in a comparably short time.^{3,9} Therefore, the ionic conductivity, also referred to as

the Li-ion diffusion kinetics, needs to be maximized.^{10–12} At the same time, a low electron transport resistance within the active mass (AM) layer of the electrodes consisting of the active material, a polymer binder, and additives is required. For this reason, the active material particles need to have good electrical contact to each other and to the current collector.

In order to ensure a low electron transport resistance of the electrodes and to increase their energy density, active mass loading is preferably increased and after the drying process, this active mass layer is highly compacted by a calendaring process.^{10,13,14} However, strong compaction of the active mass layer negatively affects its ionic conductivity, which is mainly defined by porosity and tortuosity. These pores act as transport channels for the Li-ions and contribute to the ion mobility within this layer. In addition to the ionic conductivity within the active mass layer, a higher amount of pores increases the interface area between the electrolyte and the active material particles and, thus, enhances the exchange of

Li-ions between the solid active material and liquid electrolyte phase.^{10,15}

Besides an overall reduction of porosity and pore size during the calendaring of cathodes based on the NMC111 ($\text{Li}(\text{Ni}_{0.33}\text{Mn}_{0.33}\text{Co}_{0.33})\text{O}_2$) active material, Schmidt *et al.*¹¹ observed for highly densified samples the formation of a dense layer close to the cathode's surface with the binder-additive compound (BC) clogging most of the surface pores. Based on electrochemical tests, the authors came to the conclusion that this layer significantly deteriorates the ionic conductivity and, thus, the rate capability of the electrodes. This blocking of the Li-ion diffusion was also observed by Zheng *et al.* They detected an increase of activation energy required for the transfer of Li-ions from the liquid electrolyte into the solid active mass layer along with the compaction level of the cathode.¹⁰

The laser based selective removal of the binder-additive compound close to the surface of such cathodes was recently investigated using short pulsed laser systems with pulse durations in the nanosecond time range.^{5,16} Using near infrared laser radiation, the pores in near surface areas are reopened and can act as access points for the electrolyte. By the selective removal of the binder-additive compound clogging the pores, Bolsinger *et al.*⁵ achieved a significant increase of the fast charging ability of highly densified cathodes up to more than 20%. A more detailed investigation concerning the laser process by Ruck *et al.*¹⁶ showed that with increasing laser power, the photothermic process tends to cause thermally induced changes on the surface of the NCM111 active material particles, which might negatively affect its electrochemical properties. Moreover, applying inadequate laser parameters, the whole active mass is removed including the active material. Figure 1 sketches the

process principle derived from these investigations. As the pulsed laser radiation hits the near surface layer consisting mainly of the binder-additive compound, the superficial polymer binder is evaporated and thus removed together with the conductive additives contained therein. The heat of this photothermic process partially conducts into the active material particles. As soon as the surface of the active material particles reaches a critical temperature, their surface shows microstructural changes. The aim of the laser process described by Bolsinger *et al.*⁵ is to operate selectively without affecting the active material. Thus, it is of great importance to better understand the evolution of the temperature within the electrode to be able to control the laser process accordingly.

Due to the short laser interaction times within the nanosecond range, the *in situ* measurement of the temperature during this laser process would require a highly elaborated experimental setup. Within this paper, we propose a numerical approach to describe the temporal and spatial progression of the workpiece temperature during laser material processing. This thermophysical approach is designed to be applicable to selective laser ablation processes of multilayer and multiphase materials, in general, but we concentrated on NMC111-based cathodes for Li-ion batteries. In addition to the prediction of the depth of the selectively removed binder-additive-phase, the model's intention is also to allow evaluation of the thermal impact on the active material particles. First, the general design of the thermal system is introduced for selective laser ablation processes of a multilayer workpiece such as the LiB cathode. Subsequently, the mathematical basics are described. Finally, the model is validated experimentally evaluating the evaporated volume of the binder-additive compound as well as the occurrence of thermally induced microstructural changes on the active material particles surface.

II. THERMAL PROCESS MODELING

The analytical solution of the heat conduction equation can be derived by using the Green functions. The methods of this approach and its application to laser material processing issues have been already well described in the literature.^{17,18} The applicability of these methods on ablative, ultrashort pulsed laser processes was already investigated by Weber *et al.*^{19,20}

In this paper, however, a numerical solution method is applied, which allows a comparably convenient implementation of finite workpiece dimensions and versatile temporal heating, e.g., by laser pulses that were derived from power measurements with the real laser system. In addition, infinity temperature in the solution of the heat conduction equation due to the Green function is avoided.¹⁹

A. Thermal system

Figure 2 shows the thermal system. The workpiece is in direct contact with a heat sink, e.g., current collector of the electrode and the machine table that, due to its high thermal mass, is assumed to have a constant temperature T_0 . The workpiece—the cathode—itself is approximated by two separate solid layers (layers I and II). Following Refs. 5, 11, and 16, layer I (BC layer) is assumed to consist only of polymer binder (50 wt. %) and conductive additives (50 wt. %). Layer II (AM layer) represents the active mass with a given composition of the active material, polymer binder, and

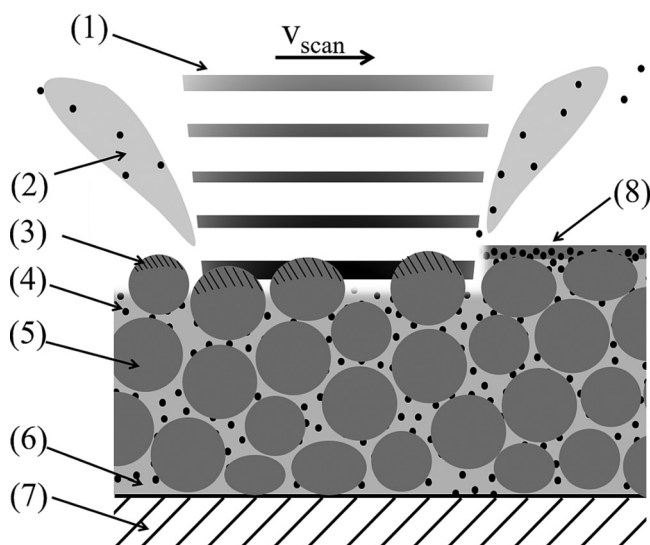


FIG. 1. Working principle of the selective laser removal process of polymer binder from lithium-ion battery cathodes: (1) pulsed laser radiation, (2) evaporated binder, (3) thermal impacts on active material particles, (4) conductive additive, (5) active material particle, (6) binder network, (7) current collector, and (8) binder-additive surface layer in accordance to Ref. 16.

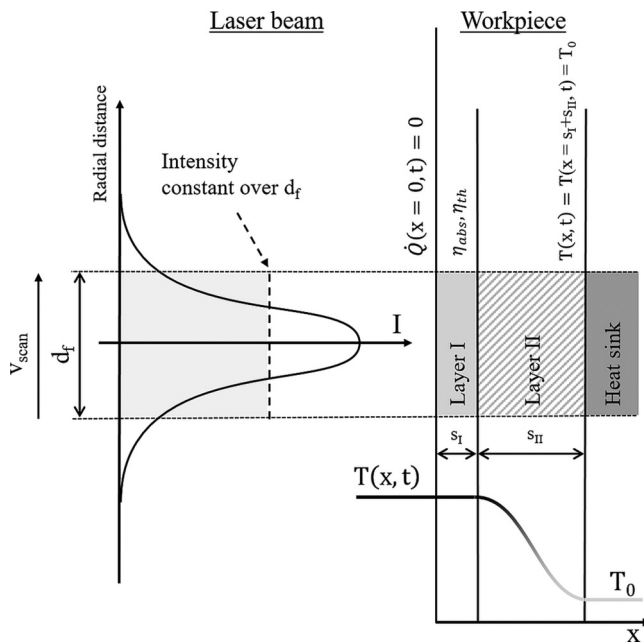


FIG. 2. Schematic sketch of the system used for the thermophysical modeling of the selective laser ablation process.

conductive additives. We assume that the different materials are homogeneously distributed and describe the properties of layers I and II as homogenized properties. The calculation of the properties will be described in Sec. II B.

The interfaces between both material layers and the heat sink are assumed to be ideal without any additional thermal transfer resistances. During the laser processing, the pulsed radiation is focused on top of the workpiece at $x=0$ with a focal diameter d_f and a Gaussian intensity distribution. The underlying laser process, as it was described by Refs. 5 and 16, operates with a relative motion between the laser beam and the workpiece surface. The direction is shown as v_{scan} in Fig. 2. In the present case, this non-stationary three dimensional process is transferred to a static one by assuming a spatially constant intensity (top-hat) distribution over the entire diameter of the laser beam, marked as a dashed line in Fig. 2. The interaction time between the laser and the workpiece T_{interact} is defined as the time required by the laser to pass the distance of one focal diameter d_f at a given scanning velocity v_{scan} .

The laser radiation interacts in this model with a volume V_{interact} that is defined by the area of the laser spot and the depth s in which the laser radiation is absorbed. This depth depends on the absorption properties of the materials in layers I and II. As indicated in Fig. 2, the absorption properties are facilitated by an absorption efficiency η_{abs} representing the fraction of the laser radiation that is absorbed either entirely in layer I or in both layers to a certain fraction. The latter case will appear if layer I is partially transparent for the incident laser radiation. In the present case, polyvinylidene difluoride (PVDF) that was used as binder in the investigated cathodes is highly transmitting near infrared wavelengths.²¹

However, due to the carbon black (CB) contained within layer I, we assume that this layer becomes highly absorbing. As the literature states, carbon black only transmits 1.5% of the incident radiation.^{22,23} The typical particle diameter of the carbon black powder is in the lower nanometer range. Presupposing a surface layer with a thickness of several carbon black particle diameters, a layer thickness of $1\mu\text{m}$ is sufficient to absorb the entire laser radiation within layer I. This leads to an absorption efficiency of $\eta_{\text{abs}}=1$. Hence, layer I is considered to act as the interaction volume V_{interact} . The absorption efficiency and all thermophysical material properties are treated in a similar way as in the literature^{19–21} and are thereby assumed to be independent of temperature, time, and space.

In addition to the first boundary condition that is defined by a constant temperature of the heat sink, a second one at the surface of the workpiece needs to be added in order to solve the heat conduction equation. Therefore, the interface between the top layer of the workpiece and the ambient air is assumed to only exhibit a negligible heat transfer.

The investigated selective laser process is meant to remove the material by evaporating the polymer binder and thus removing the binder-additive compound layer (layer I) and, partially, the binder-additive compound contained within the active mass layer beneath as well. According to the investigations of Weber *et al.*,^{19,20} the energy that is required for the phase transitions can be taken into account by introducing a thermal efficiency coefficient η_{th} as it is shown by Eq. (1). It summarizes the enthalpies for the transitions from solid to liquid h_{melt} and from liquid to gaseous phase h_{evap} together with the related volumes V_{melt} and V_{evap} . Since the evaporated material will partly exceed the evaporation temperature, an additional heat Q_{vapor} will be lost for the process and affect its efficiency.¹⁹ The thermal efficiency η_{th} is finally determined with the laser pulse energy E_{pulse} that is being absorbed within the interacting volume,

$$\eta_{\text{th}} = 1 - \frac{V_{\text{melt}} \cdot h_{\text{melt}} + V_{\text{evap}} \cdot h_{\text{evap}} + Q_{\text{vapor}}}{\eta_{\text{abs}} \cdot E_{\text{pulse}}}. \quad (1)$$

B. Physical approach

Heat transfer results from the energy transport mechanisms conduction, convection, and radiation. In most cases when solids are concerned, the fraction of convection and radiation is negligible.¹⁷ Nevertheless, regarding laser processes like laser welding where a significant amount of the workpiece material is transferred into a liquid phase, convection needs to be taken into account for the calculation of temperature fields.^{18,24} However, due to the low decomposition temperature of PVDF and the laser processing with nanosecond pulses, the energy fraction being transported by convection is assumed to be negligible compared to the heat conduction within the solid material.^{8,25} The mathematical description of the thermal system was, therefore, done by using only the heat conduction equation for solids. This equation is already known for being applicable to solving thermal problems resulting from laser material processing.^{18–20,24,25} Equation (2) depicts the heat conduction equation being able to describe temperature fields resulting from the transient three dimensional heat flow in a Cartesian coordinate system,¹⁷ where k is the temperature conductivity, c_p is the

specific heat capacity, and ρ is the density of the workpiece,

$$\frac{\partial T}{\partial t} = k^* \left(\frac{\partial^2 T}{\partial x^2} + \frac{\partial^2 T}{\partial y^2} + \frac{\partial^2 T}{\partial z^2} \right) + \frac{w(t)}{c_p^* \rho}. \quad (2)$$

According to the convention of Hgel and Graf²⁴ and Bliedner *et al.*,²⁵ heat flows can be regarded as one dimensional as long as the thermal diffusion length l_{th} that is defined by $2\sqrt{k^* t_{interact}}$ is small compared to the size of the heat source. In other words, for $l_{th} \ll d_f$, the assumption of an one dimensional heat flow delivers acceptable accuracy compared to the three dimensional solution while being far less elaborate.^{18,25} Regarding l_{th} and d_f of our use case, it is admissible to utilize the one dimensional consideration of the heat flow. Applying this simplification to the heat conduction equation leads to Eq. (3), including the above described concept of the thermal system,

$$\frac{\partial T}{\partial t} = k^* \frac{\partial^2 T}{\partial x^2} + \frac{\eta_{abs}^* \eta_{th}^* w_{interact}(t)}{c_{p,interact}^* \rho_{interact}}, \quad (3)$$

where $w_{interact}(t) = P_L(t)/V_{interact}$ represents the homogeneously spread power density within the interaction volume caused by the time dependent power of the pulsed laser radiation $P_L(t)$. $P_L(t)$ is predominantly defined by the pulse repetition rate, pulse duration, pulse shape, and the diode pump power of the laser source. The temperature λ_{eff} , the density, and the specific heat capacity of the workpiece material is shown as

$$k = \frac{\lambda_{eff}}{\rho^* c_p}. \quad (4)$$

The solution of the parabolic partial differential equation was conducted by using the *ODE15* solver being part of the software *MATLAB/Simulink* (The Mathworks, Inc.). This solver is based on the Numerical Differentiation Formulas as they were described by Klopfenstein *et al.*²⁶ Their application within the *ODE15* solver has already been well investigated by Shampine and Reichelt.²⁷

The solution of Eq. (3) asks for the mathematical description of the boundary and initial conditions in order to fully define the resulting temperature field.^{18,28} The initial state of temperature at $t = 0$ is defined to be equal to room temperature T_0 for all x . On the surface of the workpiece, the heat flow that is equal to zero is defined by using the Neumann boundary condition,¹⁸

$$k^* \frac{\partial T}{\partial x} = 0. \quad (5)$$

Vice versa, the constant temperature at the lower end of the workpiece—the interface with the heat sink—can be declared by using the Dirichlet formulation,

$$f(x, t, T) - T_0 = 0. \quad (6)$$

One major aspect that has a significant impact on the workpiece temperatures is its thermal conductivity. Looking at the subsequent application of the model reveals that the active mass layer (layer II in Fig. 2) is a multiphase material consisting of the active

material particle (A) phase and the surrounding binder compound (B) phase formed by the polymer binder, carbon black powder, and pores. The B phase is forming a matrix that is embedding the particle phase. Considering highly compacted cathodes the active material particles are in direct contact with each other. This leads to two interpenetrating networks—the particle network and the binder-additive-pore network. In such multiphase materials, the effective thermal conductivity of the entire compound can be approximated in several different ways.^{29–32} Collishaw and Evans³¹ already gave a comprehensive summary of these methods. In theoretical considerations of the thermal and electrochemical behavior of LiB-cathodes during operation, the Bruggemann equation is widely used.²⁹ For the sake of complexity reduction, we used a simplified model for the approximation of the effective thermal conductivity of the active mass compound and the binder-additive compound. As described by Smith *et al.*,³⁰ the volumetric rule of mixtures can be well applied for the estimation of the effective thermal conductivity of multiphase compounds. As shown in Eq. (7), it considers the volumetric fractions v and thermal conductivities λ of the different phases A and B,

$$\lambda_{eff} = v_A^* \lambda_A + v_B^* \lambda_B. \quad (7)$$

The effective thermal conductivity of the binder-additive-pore network was approximated using the volumetric rule of mixtures as well, including air contained within the pores as a third phase. The volumetric fractions correspond to the cathode setup used for the experimental investigations.

III. EXPERIMENTAL SETUP

The necessary experiments to calibrate and validate the calculation model were performed using the subsequently described setup.

A. Material setup

The experimental investigations were performed with industrially produced cathodes (CustomCells Itzehoe GmbH). Their active mass layer consisted of 90 wt. % lithium-nickel-manganese-cobalt-oxide [Li(Ni_{0.3}Mg_{0.3}Co_{0.3})O₂, also known as NCM111 or NCM] as the active material, 5 wt. % PVDF as a polymer binder and 5 wt. % CB as conductive additive. This active mass was coated onto a 18 μ m thick aluminum foil used as current collector, dried and calendered afterward. The resulting cathode had an energy density of 3.5 mAh/cm² at an overall porosity of 35%. The active mass layer had a thickness of 104 μ m. Table I summarizes the thermophysical properties of the single components of the active mass layer.

In addition to the industrially produced cathodes, separate samples consisting of 50 wt. % PVDF solved in *n*-methyl-2-pyrrolidone (NMP) and 50 wt. % CB were built by mixing the suspension for 2 h and the subsequent application of the liquid compound with a doctor blade coating device onto an aluminum plate. After drying for 24 h at ambient air under an extractor hood, the coating was 118 μ m thick. All thicknesses were measured by white-light interferometry. The pure BC samples were used to determine the ablation threshold of pure BC, which is required for the derivation of the thermal efficiency coefficient.

TABLE I. Thermophysical properties of the active material compound layer components (Refs. 33–37).

	PVDF	CB	NCM
Density, ρ (kg/m ³)	1778	2250	3180
Specific heat capacity, c_p (J/kg K)	1250	710	1172
Thermal conductivity, λ (W/mK)	0.275	169	0.2

B. Laser treatment

The laser experiments were conducted with a TruMark5020 Yb-fiber laser (Trumpf). The laser is operating at a wavelength of 1060 nm and a beam quality of $M^2 < 2.0$. Within these investigations, the pulse duration was varied from 9 up to 200 ns. The laser beam was focused on the workpiece surface using a 2D scanner optic with a focal length of 160 mm resulting in a focal diameter of approximately 70 μm . All laser treatments were performed under ambient air with no process gas and a constant scanning velocity of 1.5 m/s. In order to determine the ablation threshold, the scanner was performing single tracks with a line length of 1000 μm and a hatch distance of 500 μm . For all other experiments, the hatch distance was set to 35 μm . Attention was paid to ensure a plane surface of the workpiece during the laser processing.

C. Measurement of laser power and pulse shape

The measurement of the time dependent laser power $P_L(t)$ was conducted according to DIN EN ISO 11554:2017-12.³⁸ The pulse energy and average laser power were gauged using the Powermax-RS thermopile together with the LabMax-Pro SSIM power and energy meter (Coherent, Inc.). The shape of the pulse was determined by applying the laser beam perpendicularly onto the ThorLabs DET10A photodetector delivering a voltage proportional to the incident laser power. This signal was processed using a Teledyne Lecroy HDO600A digital oscilloscope allowing the record of 10^9 samples per second. The scaling of the voltage progression of the photodiode to the real laser power was done by using the single pulse energies resulting from the energy measurements.

D. Microstructural analysis

The ablation depth was determined with a Zygo NewView 8300 white-light interferometer (WLI). For the single track ablation threshold investigation, the average line depth was determined with the mean depth of three single lines. Each measurement line had a length of 500 μm and was placed inside and parallel to an ablated track. The surrounding untreated surface was used as reference height. Using the same WLI, the laser induced change of the areal roughness profile height S_z of the cathode (in the following considered as surface roughness) was determined by measuring the roughness profile of a laser treated and an untreated square area next to it, each with a side length of 400 μm . The difference between the measurement results of both areas is ascribed to the laser treatment. It was taken care of capturing measurement areas with no irregularities deteriorating their representativeness.

Moreover, due to its size, each measurement area represents a multitude of laser scanning lines.

A Zeiss LEO Gemini 1525 scanning electron microscope (SEM) was utilized to analyze the changes within the cathodes microstructure resulting from the laser treatment. Therefore, circular samples with a diameter of 10 mm were cut out of the cathode foil with an MSK-T-07 disc cutter.

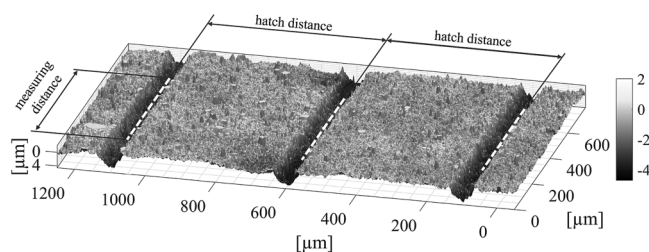
IV. RESULTS AND DISCUSSION

The experimental results are split into two successive steps. First, the thermal efficiency coefficient was determined indirectly by ablation threshold measurements and subsequent simulation of the threshold parameter setup. The thermal efficiency is an input quantity for the calculation of the resulting temperature within the interaction zone (layer I) and the temperature distribution within the active mass (layer II). The second step is the validation of the model concerning the removal of the BC layer, the prediction of the depth in which binder-additive compound is removed from the active mass layer, and the evaluation of thermally induced microstructural changes on the active material particle surface.

A. Model calibration

Figure 3 exemplarily depicts an excerpt of a white-light interferometer image of a laser treated pure binder-additive compound sample. The three dashed white lines in the figure represent the lines being used for the determination of the average line depth. It can be seen that they are sufficiently separated to use the untreated flat area between them as reference height.

The results of the average line depth of all samples are shown in Fig. 4 as a function of average laser power. It can be seen that for an average power ≥ 0.9 W, a measurable ablation of the binder-additive compound took place. Less or equal to 0.55 W negative ablation depth occurred, indicating an increase of volume of the compound within the interaction zone of the laser. Due to the low melting temperature of PVDF of 179 $^{\circ}\text{C}$,³⁹ this might be caused by foaming of the thermoplastic binder similar to a laser marking process.²⁵ The transition from that “foaming” regime to the evaporation regime leads to the conclusion that the ablation threshold of the binder-additive compound is approximately at 0.75 W average laser power, i.e., an energy per unit length of 0.5 J/m using a

**FIG. 3.** Excerpt of a WLI image of a single track laser treated pure binder-additive compound sample being processed with an average laser power of 2.8 W, a pulse duration of 9 ns, and a pulse repetition rate of 200 kHz.

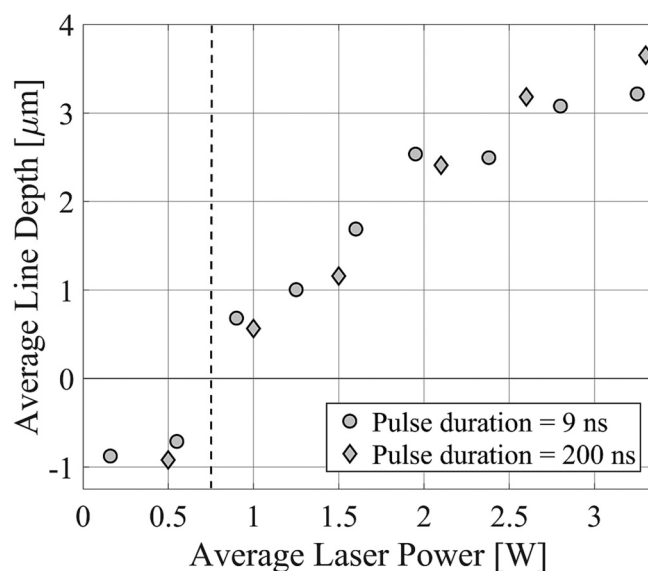


FIG. 4. Ablation depth as a function of average laser power and pulse duration of the pure binder-additive compound performed with a constant pulse repetition rate of 200 kHz and a scanning speed of 1.5 m/s. The ablation threshold is indicated with a vertical dashed line.

scanning velocity of 1.5 m/s as marked by the dashed line in the figure. Moreover, the results show that this threshold is the same for both pulse durations of 9 and 200 ns.

The approximation of η_{th} was conducted indirectly by implementing this threshold laser parameter into the calculation model. For this use case, the model also consisted of two layers, both having the identical thermophysical properties of BC. Here, layer I with a thickness identical to one of the BC layers of the cathode model was also used as the interaction volume absorbing the entire laser radiation. The laser power $P_L(t)$ required as the input value for $w_{interact}(t)$ was determined by power measurements of the ablation threshold laser parameters with the average laser power of 0.5 W. Afterward, the value of η_{th} being part of the heat conduction equation was iteratively adjusted until the maximum peak temperature exceeded the average decomposition temperature of PVDF [$T_{decomp,BC} = 300^\circ\text{C}$ (Ref. 4)]. The decomposition temperature was used because it is stated by the literature⁸ that the decomposition of PVDF leads to the evaporation of the binder material. With the given scanning velocity, pulse duration, and pulse repetition rate, the model workpiece is exposed to ten laser pulses during the interaction time of $46.3\mu\text{s}$, which is represented by the vertical dotted line in Fig. 5. Each pulse results in a temperature peak. Setting the thermal efficiency to 71% led to a calculated temperature progression on the surface of the binder-additive sample as displayed in Fig. 5. The calculated maximum peak temperature of 304°C , resulting from the incident laser pulses during the interaction time, exceeds the decomposition temperature, which is marked by the horizontal dashed line. The exceedance of the decomposition temperature at the last laser pulse is the first indicator for a beginning

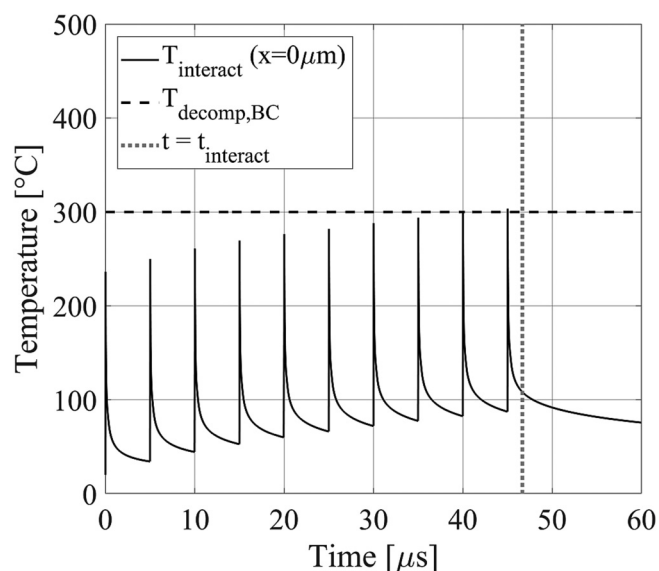


FIG. 5. Calculated progression of the temperature of the interaction zone of the binder-additive compound sample using an average laser power of 0.75 W, a pulse duration of 9 ns, a repetition rate of 200 kHz, and a scanning velocity of 1.5 m/s together with a thermal efficiency of 71%.

material removal. For this reason and because the laser parameters of the ablation threshold were used, we utilized this criterion to determine the thermal efficiency. The usage of the ablation threshold also means that the thermal efficiency does not take into account the energy that is stored within the ablated material, meaning that Q_{vapor} in Eq. (1) is set to zero.

B. Prediction of the selective removal of the binder-additive surface layer

The validation of the thermophysical model concerning the prediction of the selective removal of the superficial BC layer (layer I) was conducted by the laser treatment of NCM cathodes and the subsequent comparison with the calculation results. Similar to the ablation threshold investigation with the binder-additive compound, two different pulse durations (9 and 200 ns) and several average laser power levels ranging from 0.7 up to 10.8 W, i.e., energies per unit length from 0.47 up to 7.2 J/m were applied.

Figure 6 depicts top-view SEM images of the untreated cathode surface in low magnification (a) and in detailed view (b) as a reference. Figure 6(a) demonstrates that even on these comparably moderately densified cathodes with a porosity of 35%, the major surface area is covered with the binder-additive compound referred to as the BC layer. As a consequence, most of the surface pores are clogged and only a few active material particles are easily accessible for the Li-ions on the top surface as shown in Fig. 6(b).

Figure 7 shows top-view SEM images of laser treated samples using a pulse duration of 9 ns, each at two different magnifications. The left column shows the transition from the laser treated surface

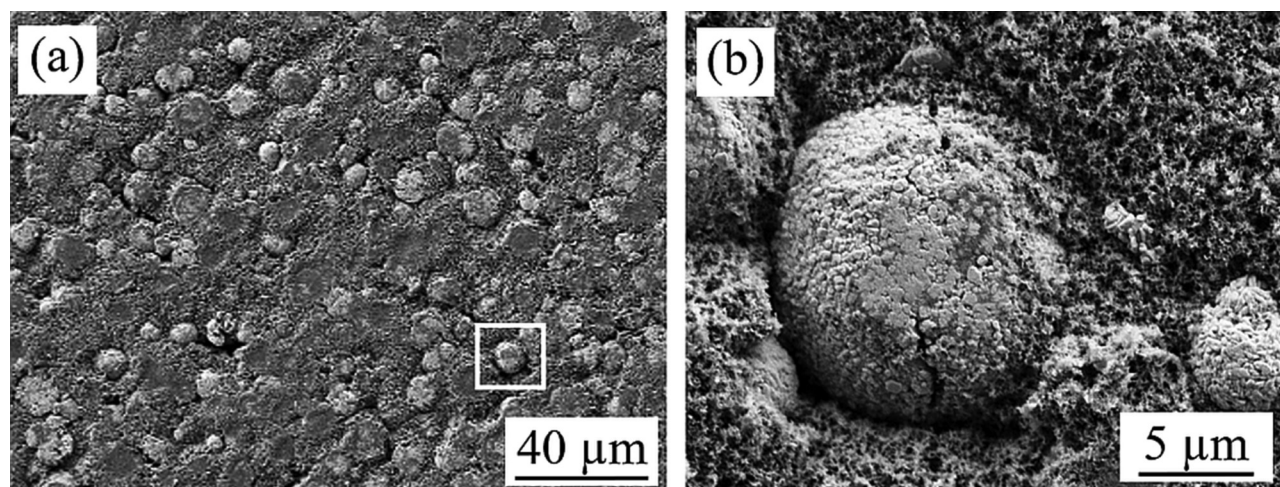


FIG. 6. Top-view SEM images of an untreated cathode surface (a) and a detailed image of a single untreated NCM particle surrounded by the binder-additive compound (b).

above the dashed line to the untreated reference surface below the dashed line. The right column depicts an excerpt from the center of the laser treated area.

At a first glance, the right image in the upper row is comparable to Fig. 6(b) and shows that an energy per unit length of 0.37 J/m causes hardly any removal of the binder-additive compound. However, having a closer look at the transition between the laser treated and the untreated surface reveals that this energy per unit length already leads to a decent removal of the BC layer. From 0.53 J/m onward, this is much more pronounced and increases along with the energy per unit length. In comparison with the results of the ablation threshold for pure BC, the removal of BC using cathodes (instead of the pure binder-additive compound) requires far less energy per unit length. This might be attributed to the different thermophysical properties of the pure binder-additive samples compared to the entire cathodes used in the present investigation, such as the effective thermal conductivity. For the pure BC, this results in 74.75 W/mK, whereas the effective thermal conductivity for the active mass layer (layer II) is only 45.16 W/mK. This difference leads to a reduced process energy loss when treating the cathodes and thus a lower threshold energy for the ablation of the binder-additive compound layer.

The implementation of the laser parameters corresponding to (a) into the model for the entire cathode led to the evolution of the temperature $T_{interact}$ within the interaction zone (layer I) as displayed in Fig. 8. The decomposition temperature of PVDF is exceeded at the fifth laser pulse, where the temperature within the interaction zone reaches 301 °C. The temperature reaches a maximum of 356 °C with the last pulse. This is in agreement with the decent removal of the BC surface layer that was discovered in the SEM pictures in Fig. 7(a). Of course, the temperature of the interaction zone is increasing along with the energy per unit length that is applied to the workpiece.

In contrast to reality, the volume of the workpiece in the simulation remains constant over the entire time that is considered.

Therefore, the calculated temperatures exceeding the decomposition temperature need to be considered carefully because the thermal efficiency coefficient including the absorption properties η_{th} and the fraction of energy stored within the ablated material Q_{Vapor} will change as soon as the decomposition temperature of the BC layer is exceeded, and this layer is removed. It will be shown later that not taking this aspect into account will still allow sufficiently accurate results while enabling very efficient solution methods without a continuous remeshing of the workpiece model. Furthermore, considering the continuously changing workpiece would require additional experimental investigations concerning the thermal efficiency of the active mass layer.

Figure 9 depicts SEM images of samples that were treated with a pulse duration of 200 ns, a scanning velocity of 1.5 m/s, a pulse repetition rate of 200 kHz, and an average laser power of 0.7 W, i.e., an energy per unit length of 0.47 J/m. The transition from the untreated to the treated area reveals that the top layer of the binder-additive compound is being removed by the laser process. According to the calculation, these laser parameters cause a maximum peak temperature of 390 °C within the interaction volume, i.e., the BC layer, which is also above the decomposition temperature of PVDF.

C. Estimation of the removal depth of the binder-additive compound

Regarding the surface topology of the cathodes, one can conclude that the roughness will consequently increase due to the selective removal of the binder-additive compound as long as no significant removal of active material particles takes place. The laser induced change of surface roughness of the samples in respect of the energy input is evaluated in Fig. 10 (left ordinate axis). For an energy input below 2.5 J/m, there is a linear correlation with the surface roughness. Similar to the ablation threshold measurement of the pure binder-additive compound, this relation seems to be

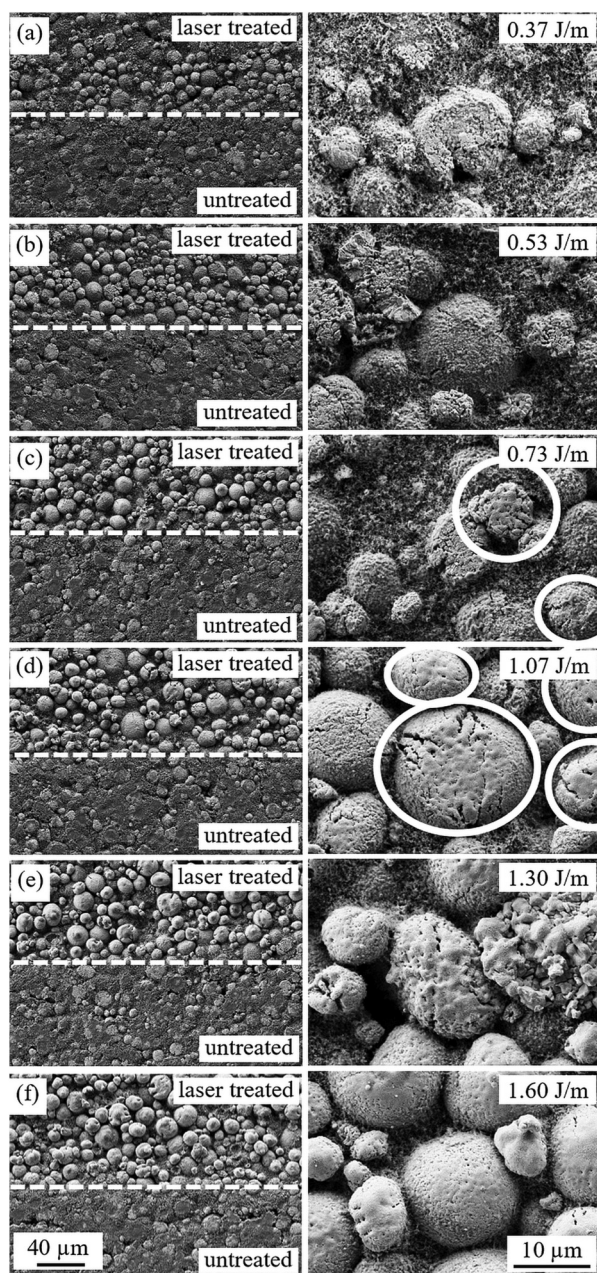


FIG. 7. Top-view SEM images of cathodes being laser treated with an energy per unit length of 0.37 J/m (a), 0.53 J/m (b), 0.73 J/m (c), 1.07 J/m (d), 1.30 J/m (e), and 1.60 J/m (f) at constant pulse durations of 9 ns and a pulse repetition rate of 200 kHz. The dashed line marks the transition from the laser treated surface area (above) to the untreated area (below).

independent of the pulse duration. For energies >2.5 J/m, a kind of step is formed at pulse durations of 9 ns, whereas at 200 ns, the linear behavior continues up to 4 J/m. Regarding the 9 ns pulses, the linear progression reappears in an energy range between 4 J/m

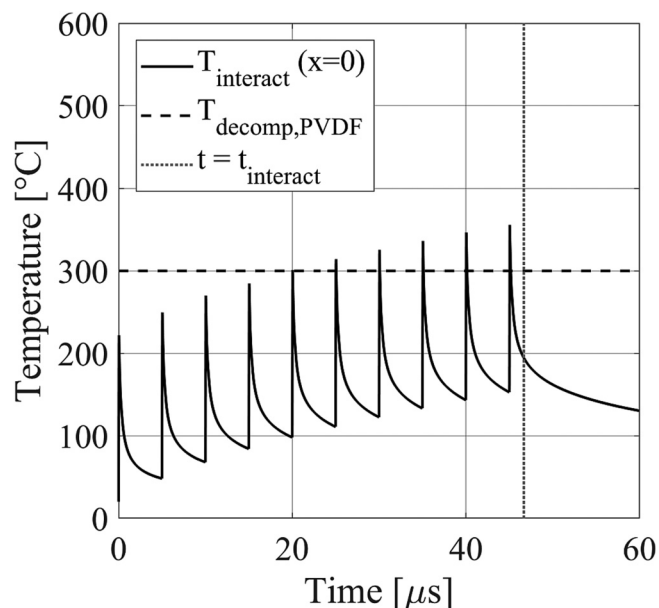


FIG. 8. Calculated temperature progression within the interaction zone $T_{interact}$ applying 0.37 J/m at a repetition rate of 200 kHz.

and the maximum energy input available for this laser configuration of 5.5 J/m. Pulse durations of 200 ns led to a pronounced plateau at a laser energy input >4 J/m.

These nonlinearities such as the step for a pulse duration of 9 ns and the plateau for 200 ns might be ascribed to the beginning of the removal of active material particles either by direct ablation or indirectly by the vapor pressure of the binder tearing out the particles. This phenomenon could already be observed within the investigations of Ruck *et al.*¹⁶ Using the identical laser system as in the present study, they applied a proportion of diode pump power of 60% at a pulse duration of 9 ns, a pulse repetition rate of 200 kHz and the identical scanning velocity. The top-view SEM images that were presented, showed that the energy per unit length of 2.81 J/m causes spherically shaped craters within the NCM based cathode surface. Due to the size and shape, these craters might be ascribed to the removal of active material particles.

Due to the proportionality between energy and temperature in general, a correlation between the depth of vaporized binder (the surface roughness) within the active mass layer and the propagation depth of the decomposition temperature was expected. This means that the volume in which the peak temperature exceeds the decomposition temperature of PVDF (V_{pen}) is assumed to be equal to the evaporated BC volume. Because of the assumption of an ideal selective process, the active material particles are supposed to remain part of the workpiece. Thus, the residual volume of the cathode V_{res} can be written as follows:

$$V_{res} = V_{cathode} - V_{pen} \cdot v_r \quad (8)$$

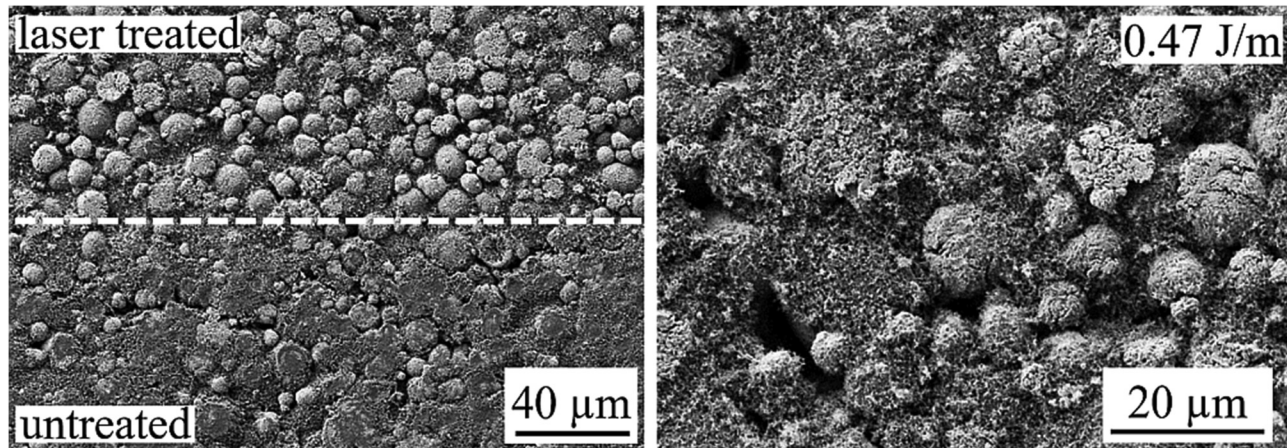


FIG. 9. Top-view SEM images of samples that were treated with an energy per unit length of 0.47 J/m, a pulse duration of 200 ns, and a pulse repetition rate of 200 kHz. Left: transition between the laser treated area (above the dashed line) and the untreated area (below). Right: detailed image of the center of the laser treated area.

where $V_{cathode}$ represents the initial volume of the entire active mass layer and v_r is the volumetric fraction of the removed material within the thermally critically penetrated volume V_{pen} . Because of the one dimensional consideration and the assumption of a constant surface area, the volume can be reduced to the depth in which the decomposition temperature is exceeded (x_{pen}). Together with the ablation threshold $E_{Dis,th}$, the average depth in which the binder is removed x_{vapor} , i.e., the theoretical surface roughness profile height can be defined according to Eq. (9),

$$x_{vapor} = \begin{cases} 0, & E_{Dis} < E_{Dis,th} \\ v_{pen} * (1 - v_r), & E_{Dis} \geq E_{Dis,th} \end{cases} \quad (9)$$

As shown in Fig. 10, this very simple approach of estimating the average ablation depth of one single component led to a good agreement between the calculated depth of evaporated BC and the measured change of surface roughness. Presupposing that the surface roughness is a measure for the removal depth of the binder-additive compound, the thermophysical based calculation delivers sufficiently accurate results within the linear process range below 2.5 J/m for 9 ns and 4.1 J/m for 200 ns, respectively. A change of surface roughness $>15 \mu\text{m}$, i.e., one average particle diameter is not desirable anyway since this indicates removal of active material and thus a reduction of the maximum achievable cell capacity. This good correlation within the lower energy range also gives reason to suppose that within this range, the energy fraction of Q_{vapor} contributing to the thermal efficiency coefficient does not have a significant impact on the temperature within the workpiece. Apart from that, this agreement further reinforces the assumption of the selective operating principle of the laser treatment process.

The slight deviations within the linear process range between the calculated evaporation depth which implies an ideal selective process ($v_r = v_{r,BC}$) and the real depth of material removal are likely to indicate either an energy loss due to Q_{vapor} or removal of additional material and thereby a not fully selective process. For

example, removal of smaller active material particles (A) that are easily torn out of the active mass layer due to the vaporization pressure would require an increase of v_r by a certain fraction $v_{r,A}$ according to Eq. (10).

$$v_r = v_{r,BC} + v_{r,A} \quad (10)$$

The assumption of $v_r = v_{r,BC}$ also causes a pronounced discrepancy between simulation and the real measurement at higher energy inputs per unit length. As already indicated by the spherical craters observed in the SEM images, higher energy inputs lead to a removal of the entire active mass. Thus, $v_r = v_{r,BC}$ is not valid in this range. A fraction of removed active material must be added according to Eq. (10). Moreover, the removal of the entire active

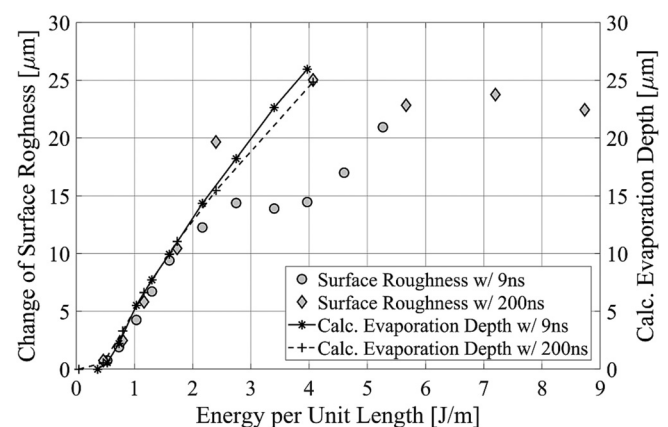


FIG. 10. Comparison of the measured change of surface roughness on the left ordinate and the calculated evaporation depth on the right ordinate as a function of energy per unit length.

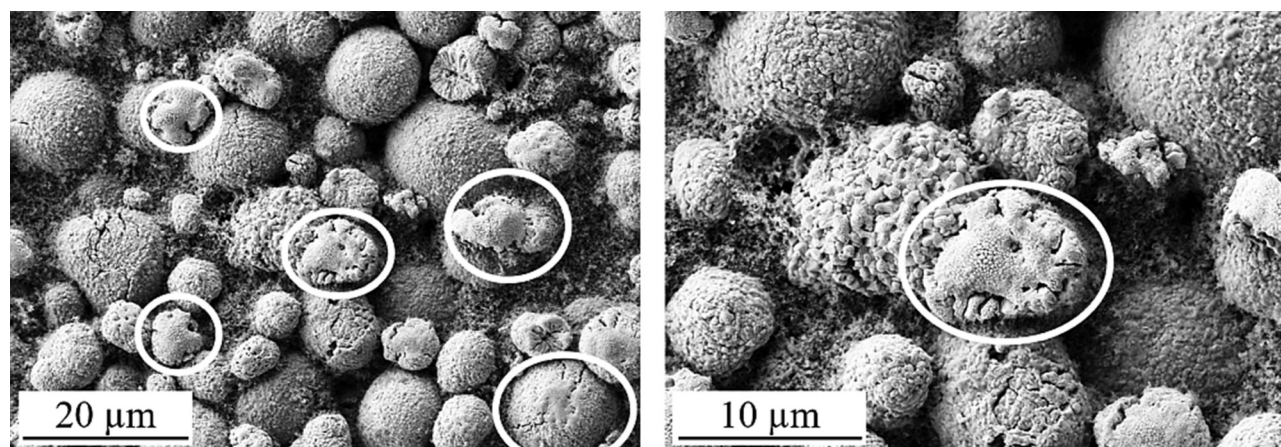


FIG. 11. Top-view SEM images of cathodes treated with an energy per unit length of 0.8 J/m, a pulse duration of 200 ns, and a pulse repetition rate of 200 kHz.

mass is likely to cause a non-negligible loss of process energy due to the heat contained within abated material Q_{vapor} .

D. Evaluation of thermal impacts on composite components

In the literature, the thermally induced microstructural changes on NCM particles are referred to as thermal damages¹⁶ or melt formations.⁵ A widely used production process of NCM active material includes a calcination process at about 700 °C up to 1000 °C.^{40,41} Thus, one can roughly conclude that during the selective laser treatment process, the maximum peak temperatures that occur on the surface of the active mass layer (layer II) has to exceed this temperature in order to cause thermally induced microstructural changes. Having a look at Fig. 7, it becomes obvious that such microstructural changes that might be interpreted as superficial melting locally occur at 0.73 J/m using a repetition rate of 200 kHz. The white ellipses in Figs. 7(c) and 7(d) mark these changes. For a pulse duration of 200 ns, the threshold was found to be at a similar energy per unit length of 0.8 J/m. Figure 11 shows the corresponding SEM images. A further increase of energy led to more pronounced changes.

Implementing these threshold parameters into the calculation model delivers a calculated maximum peak temperature on the surface of the active mass layer (layer II) of 513 °C. This is far below the calcination temperature and does not agree with the assumption of thermal damages or melting of NCM. One possible explanation for these deviations might be the simplification of the Gaussian intensity distribution by an ideal top-hat profile with a constant radiation intensity over the entire focal diameter. The real peak intensity of the laser beam with a Gaussian intensity distribution would be far above the intensity, which was used for the thermophysical modeling. Using a Gaussian intensity distribution will, therefore, lead to significantly higher temperature peaks in the center of the laser beam. Thus, it is likely that within this area, the local temperature is far above the calculated one and causes the observed thermal damages of the NCM.

V. CONCLUSIONS

The investigations presented in this paper gave an insight into the design of thermal systems of selective laser ablation processes. It can be stated that the established model is able to predict the removal of the binder-additive compound layer on the top surface of the cathode. In order to perform a quantitative validation of the prediction accuracy, the laser induced change of roughness profile height was introduced as an indicator for the amount of the binder-additive compound that is selectively removed from the active mass layer. Microstructural measurements of laser treated cathode surfaces revealed that, as long as no significant amount of active material particles is being removed, the roughness profile height is highly dependent on the average laser power while using a constant scanning speed. The corresponding simulations further showed that the calculated evaporation depth of the binder-additive compound is in good agreement with the measured height of the roughness profile. Moreover, this agreement substantiates the selective working principle of laser treatment.

The application of the model for the prediction of thermally induced microstructural changes that were already discovered in the literature¹⁶ revealed that the calculated workpiece temperatures are far below the real process temperatures. This leads to the conclusion that the usage of a simplified top-hat intensity profile of the laser beam as it is used for the simulation model might be more suitable for the selective ablation process than the Gaussian intensity profile as it was used for the experiments. Using a top-hat profile could prevent a local overheating of the active material particles as it is the case for the Gaussian laser beam due to its high intensity in the center.

Although several model assumptions require further verification, the model can be used to support the parameter optimization of the selective laser ablation process of the polymer binder from the LiB electrode surface to enhance its fast charging abilities. Moreover, the thermal process system that was established can be transferred to laser ablation processes of other multiphase composite materials.

ACKNOWLEDGMENTS

The authors gratefully acknowledge the support of the German Federal Ministry of Economic Affairs and Energy by funding the project “structur.E—Strukturierte Anoden für verbesserte Schnellladefähigkeit und Steigerung der Energiedichte von Lithium-Ionenbatterien” (No. 03ETE018F). Furthermore, they acknowledge the fruitful discussions of the experimental findings with Jens Sandherr and Christian Weisenberger from the Material Research Institute Aalen and Max-Jonathan Kleefoot from the Laser Application Center of Aalen University.

REFERENCES

- ¹A. Tomaszewska, Z. Chu, X. Feng, S. O’Kane, X. Liu, J. Chen, C. Ji, E. Endler, R. Li, L. Liu, Y. Li, S. Zheng, S. Vetterlein, M. Gao, J. Du, M. Parkes, M. Ouyang, M. Marinescu, G. Offer, and B. Wu, “Lithium-ion battery fast charging: A review,” *eTransportation* **1**, 100011 (2019).
- ²N. Nitta, F. Wu, J. T. Lee, and G. Yushin, “Li-ion battery materials: Present and future,” *Mater. Today* **18**, 252–264 (2015).
- ³S. Ahmed, I. Bloom, A. N. Jansen, T. Tanim, E. J. Dufek, A. Pesaran, A. Burnham, R. B. Carlson, F. Dias, K. Hardy, M. Keyser, C. Kreuzer, A. Markel, A. Meintz, C. Michelbacher, M. Mohanpurkar, P. A. Nelson, D. C. Robertson, D. Scofield, M. Shirk, T. Stephens, R. Vijayagopal, and J. Zhang, “Enabling fast charging—A battery technology gap assessment,” *J. Power Sources* **367**, 250–262 (2017).
- ⁴W. Pfleging, “A review of laser electrode processing for development and manufacturing of lithium-ion batteries,” *Nanophotonics* **7**, 549–573 (2018).
- ⁵M. Bolsinger, M. Weller, S. Ruck, P. Kaya, H. Riegel, and V. Knoblauch, “Selective surface treatment by means of IR-laser—A new approach to enhance the rate capability of cathodes for Li-ion batteries,” *Electrochim. Acta* **330**, 135163 (2020).
- ⁶T. Tsuda, N. Ando, K. Matsubara, T. Tanabe, K. Itagaki, N. Soma, S. Nakamura, N. Hayashi, T. Gunji, T. Ohsaka, and F. Matsumoto, “Improvement of high-rate charging/discharging performance of a lithium ion battery composed of laminated LiFePO₄ cathodes/ graphite anodes having porous electrode structures fabricated with a pico-second pulsed laser,” *Electrochim. Acta* **291**, 267–277 (2018).
- ⁷R. Kohler, J. Proell, M. Bruns, S. Ulrich, H. J. Seifert, and W. Pfleging, “Conical surface structures on model thin-film electrodes and tape-cast electrode materials for lithium-ion batteries,” *Appl. Phys. A* **112**, 77–85 (2013).
- ⁸W. Pfleging and J. Pröll, “A new approach for rapid electrolyte wetting in tape cast electrodes for lithium-ion batteries,” *J. Mater. Chem. A* **2**, 14918–14926 (2014).
- ⁹P. U. Kurzweil and O. K. Dietlmeier, *Elektrochemische Speicher. Superkondensatoren, Batterien, Elektrolyse-Wasserstoff, Rechtliche Grundlagen* (Springer Fachmedien Wiesbaden, Wiesbaden, 2015).
- ¹⁰H. Zheng, L. Tan, G. Liu, X. Song, and V. S. Battaglia, “Calendering effects on the physical and electrochemical properties of Li[Ni_{1/3}Mn_{1/3}Co_{1/3}]O₂ cathode,” *J. Power Sources* **208**, 52–57 (2012).
- ¹¹D. Schmidt, M. Kamlah, and V. Knoblauch, “Highly densified NCM-cathodes for high energy Li-ion batteries: Microstructural evolution during densification and its influence on the performance of the electrodes,” *J. Energy Storage* **17**, 213–223 (2018).
- ¹²Y.-H. Chen, C.-W. Wang, X. Zhang, and A. M. Sastry, “Porous cathode optimization for lithium cells: Ionic and electronic conductivity, capacity, and selection of materials,” *J. Power Sources* **195**, 2851–2862 (2010).
- ¹³S. G. Lee and D. H. Jeon, “Effect of electrode compression on the wettability of lithium-ion batteries,” *J. Power Sources* **265**, 363–369 (2014).
- ¹⁴H. Zheng, G. Liu, X. Song, and V. Battaglia, “Li[Ni_{1/3}Mn_{1/3}Co_{1/3}]O₂-based electrodes for PHEV applications: An optimization. Li[Ni_{1/3}Mn_{1/3}Co_{1/3}]O₂-based electrodes for PHEV applications: An optimization,” *ECS*, **11**, 1–9 (2008).
- ¹⁵S. Babinec, H. Tang, A. Talik, S. Hughes, and G. Meyers, “Composite cathode structure/property relationships,” *J. Power Sources* **174**, 508–514 (2007).
- ¹⁶S. Ruck, S. Enderle, M. Bolsinger, M. Weller, V. Knoblauch, and H. Riegel, “Enhancing the rate capability of highly densified Li-Ion battery cathodes by selective laser ablation,” *Proc. SPIE* **10906**, 109061D (2019).
- ¹⁷H. S. Carslaw, J. C. Jaeger, L. R. Ingersoll, O. J. Zobel, A. C. U. Ingersoll, and J. H. van Vleck, *Conduction of Heat in Solids and Heat Conduction*, Bd. 1 (Oxford University, New York, 1948).
- ¹⁸R. Poprawe, *Lasertechnik für die Fertigung. Grundlagen, Perspektiven und Beispiele für den innovativen Ingenieur; mit 26 Tabellen. VDI-Buch* (Springer, Berlin, 2005).
- ¹⁹R. Weber, T. Graf, P. Berger, V. Onuseit, M. Wiedenmann, C. Freitag, and A. Feuer, “Heat accumulation during pulsed laser materials processing,” *Opt. Express* **22**, 11312–11324 (2014).
- ²⁰R. Weber, T. Graf, C. Freitag, A. Feuer, T. Kononenko, and V. I. Konov, “Processing constraints resulting from heat accumulation during pulsed and repetitive laser materials processing,” *Opt. Express* **25**, 3966–3979 (2017).
- ²¹E. Bormashenko, R. Pogreb, Y. Socol, M. H. Itzhaq, V. Streltsov, S. Sutovsky, A. Sheshnev, and Y. Bormashenko, “Polyvinylidene fluoride—Piezoelectric polymer for integrated infrared optics applications,” *Opt. Mater.* **27**, 429–434 (2004).
- ²²D. Han, Z. Meng, D. Wu, C. Zhang, and H. Zhu, “Thermal properties of carbon black aqueous nanofluids for solar absorption,” *Nanoscale Res. Lett.* **6**, 457 (2011).
- ²³A. Braeuer, Interaction of matter and electromagnetic radiation. *In situ Spectroscopic Techniques at High Pressure. Supercritical Fluid Science and Technology* (Elsevier, New York, 2015), pp. 41–192.
- ²⁴H. U. Hügel and T. Graf, *Laser in der Fertigung. Strahlquellen, Systeme, Fertigungsverfahren. Aus dem Programm Fertigung* (Vieweg+Teubner, Wiesbaden, 2009).
- ²⁵J. Bliedtner, H. U. Müller, and A. Barz, *Lasermaterialbearbeitung. Grundlagen—Verfahren—Anwendungen—Beispiele* (Carl Hanser, München, 2013).
- ²⁶R. W. Klopfenstein, “Numerical differentiation formulas for stiff systems of ordinary differential equations,” *RCA Rev.* **32**, 447–462 (1971).
- ²⁷L. F. Shampine and M. W. Reichelt, “The MATLAB ODE suite,” *SIAM J. Sci. Comput.* **18**, 1–22 (1997).
- ²⁸H. D. U. Baehr and K. Stephan, *Wärme- und Stoffübertragung* (Springer, Berlin, 2013).
- ²⁹A. Vadakkepatt, B. Trembacki, S. R. Mathur, and J. Y. Murthy, “Bruggeman’s exponents for effective thermal conductivity of lithium-ion battery electrodes,” *J. Electrochem. Soc.* **163**, A119–A130 (2016).
- ³⁰D. S. Smith, A. Alzina, J. Bourret, B. Nait-Ali, F. Pennec, N. Tessier-Doyen, K. Otsu, H. Matsubara, P. Elser, and U. T. Gonzenbach, “Thermal conductivity of porous materials,” *J. Mater. Res.* **28**, 2260–2272 (2013).
- ³¹P. G. Collishaw and J. R. G. Evans, “An assessment of expressions for the apparent thermal conductivity of cellular materials,” *J. Mater. Sci.* **29**, 486–498 (1994).
- ³²K. Pietrak and T. S. Wiśniewski, “A review of models for effective thermal conductivity of composite materials,” *J. Power Technol.* **95**, 14–24 (2015).
- ³³W. N. dos Santos, C. Y. Iguchi, and R. Gregorio, “Thermal properties of poly(vinylidene fluoride) in the temperature range from 25 to 210°C,” *Polym. Test.* **27**, 204–208 (2008).
- ³⁴H. Kuchling, *Taschenbuch der Physik* (Carl Hanser, München, 2011).
- ³⁵F. Richter, P. J. S. Vie, S. Kjelstrup, and O. S. Burheim, “Measurements of ageing and thermal conductivity in a secondary NMC-hard carbon Li-ion battery and the impact on internal temperature profiles,” *Electrochim. Acta* **250**, 228–237 (2017).
- ³⁶P. Taheri and M. Bahrami, “Temperature rise in prismatic polymer lithium-ion batteries: An analytic approach,” *SAE Int. J. Passeng. Cars Electron. Electr. Syst.* **5**, 164–176 (2012).

- ³⁷Y. Zhao, Y. Patel, T. Zhang, and G. J. Offer, "Modeling the effects of thermal gradients induced by tab and surface cooling on lithium ion cell performance," *J. Electrochem. Soc.* **165**, A3169–A3178 (2018).
- ³⁸11554. Optik und Photonik—Laser und Laseranlagen. Prüfverfahren für Leistung, Energie und Kenngrößen des Zeitverhaltens von Laserstrahlen (ISO 11554:2017)
- ³⁹Z. Liu, P. Maréchal, and R. Jérôme, "Melting and crystallization of poly(vinylidene fluoride) blended with polyamide 6," *Polymer* **38**, 5149–5153 (1997).
- ⁴⁰A. Habibi, M. Jalaly, R. Rahmanifard, and M. Ghorbanzadeh, "The effect of calcination conditions on the crystal growth and battery performance of nano-crystalline $\text{Li}(\text{Ni}_{1/3}\text{Co}_{1/3}\text{Mn}_{1/3})\text{O}_2$ as a cathode material for Li-ion batteries," *New J. Chem.* **42**, 19026–19033 (2018).
- ⁴¹J. Zheng, P. Yan, L. Estevez, C. Wang, and J.-G. Zhang, "Effect of calcination temperature on the electrochemical properties of nickel-rich $\text{LiNi}_{0.76}\text{Mn}_{0.14}\text{Co}_{0.10}\text{O}_2$ cathodes for lithium-ion batteries," *Nano Energy* **49**, 538–548 (2018).